Journal of Materials Chemistry A

A New Metal–Organic Open Framework Enabling Facile Synthesis of Carbon Encapsulated Transition Metal Phosphide/Sulfide Nanoparticle Electrocatalysts

SCHOLARONE™
Manuscripts

A New Metal-Organic Open Framework Enabling Facile Synthesis of Carbon Encapsulated Transition Metal Phosphide/Sulfide Nanoparticle Electrocatalysts[†]

Baicheng Weng, Xiaoming Wang, Corey R. Grice, Fenghua Xu, and Yanfa Yan*

Department of Physics and Astronomy and Center for Photovoltaics Innovation and Commercialization, The University of Toledo, Toledo, Ohio 43606, United States
* Email: yanfa.yan@utoledo.edu.

[†] Electronic supplementary information (ESI) available: Methods, and Supporting Figures and Tables

ABSTRACT

Engineering the $3d$ to $5d$ nonprecious transition metal electrocatalysts to demonstrate both high activity and superior durability for both the oxygen evolution reaction (OER) and hydrogen evolution reaction (HER), which would be ideal for enabling low-cost hydrogen production from water splitting, remains a serious challenge. Herein, we report a rational design and experimental realization of a new metal-organic open framework (MOF) to enable a facile and scalable synthesis of transition metal phosphide (TMP) and sulfide (TMS) composite nanoparticle electrocatalysts encapsulated by heteroatom-doped carbon (TMP/C and TMS/C) as bifunctional electrocatalysts for water splitting. Using this new MOF, we synthesized NiP/NiFeP/C and MoWS/MoP/C composite nanoparticle electrocatalysts that exhibited outstanding electrocatalytic activities and durability that are among the higher yet reported in literature for HER and OER electrocatalysts. A two-electrode water-splitting device using our bifunctional NiP/NiFeP/C catalyst reached 10 mA cm^{-2} at a cell voltage of 1.53 V and 100 mA cm^{-2} at 1.68 V in 1.0 M KOH. The device showed an excellent

stability for overall water splitting with almost 98% retention of its initial current of 100 mA cm^{-2} for over 20 h. Our results demonstrate the versatility of the new MOF to synthesize highly active and stable TM-based electrocatalysts for water splitting.

Introduction

Producing clean and recyclable hydrogen fuels by electrochemical water splitting is part of a desirable strategy to address the energy shortage and environmental pollution issues that modern society is facing.[1-6] Water splitting involves an oxygen evolution reaction (OER) and a complimentary hydrogen evolution reaction (HER).[7-22] Presently, noble metals, such as Pt, and their oxides, such as RuO_2, exhibits high efficiencies both on activities and stabilities for HER and OER, respectively.[7-22] However, their scarcity, high cost and large overpotentials at high current densities (> 50 mA cm^{-2}) significantly limit the economical viability of large-scale production of hydrogen fuels through electrochemical water splitting.[6-10] Furthermore, the use of bifunctional electrocatalysts, which have high activities for both HER and OER operation, can be desirable to simplify the design and reduce the cost of commercial water splitting devices. Extensive efforts have been made to develop active catalysts based on low-cost and earth-abundant elements, including transition metal (TM) alloys, oxides, metal-doped metal oxides, (oxy)hydroxides, phosphides and chalcogenides.[23-38] For instance, a two-step electrochemical activated oxide, Co-300/Li, shows nearly zero overpotential at reasonable OER based current densities.[36] Among them, TM phosphides (TMPs) have shown promising activities for both HER and OER, making them excellent candidates for efficient bifunctional electrocatalysts.[11-38] However, TMPs typically exhibit poor long-term stability during OER testing due to oxidation and corrosion. Encapsulation with heteroatom-doped carbon shells has been proven as an effective approach to mitigate this issue and improve the electrocatalytic activity.[27] For instance, our recent work has shown that a CoP electrocatalyst embedded in N-doped carbon matrix can achieve improved HER and OER activities.[30] The carbon matrix not only protects the CoP electrocatalyst core, but also further improves the electrocatalytic activity since N-doping enhances the conductivity of the carbon by tailoring the electron donor–acceptor behavior due to its higher electronegativity with respect to carbon.[30]

Synthesizing TMP and TM sulfide (TMS) nanostructures encapsulated in heteroatom-doped carbon matrix faces significant challenges. Metal organic compounds (*e.g.* metal organic frameworks, MOFs) have been commonly used for synthesizing core/shell nanostructures, since the metal moieties and the N- and S-containing organic linkers in the MOFs can be transformed into metal cores and doped carbon shells, respectively. Currently, the most commonly used MOFs contain 2-methylimidazole-based linkages (*e.g.* ZIF-67 and ZIF-8). But the short molecular distance between adjacent TM atoms in the

linkages may result in poor metal distributions during pyrolysis at high temperature.[29] Engineering the building blocks of the MOFs to use longer spacer molecules (ligands) provides a solution for mitigating this issue.[29] In addition, the introduction of longer N-containing ligands into the structure will induce the evolution of more desirable topology (*e.g.* larger and deformed pore structures). More importantly, the spare *d*-orbitals of vacant TM sites can coordinate additional heteroatom-containing ligands such as thiocyanide and P- containing small molecules due to weakened steric effects. The obtained MOF thus possesses advantages over conventional zeolite frameworks in introducing secondary 4*d* or 5*d* TMs (*e.g.* W and Mo, which are difficult to incorporate into most MOF structures through conventional methods) and avoiding post-synthetic phosphorization steps required to form TMPs[27-29] for zeolite framework precursors. The phosphorization process not only adds extra cost to the synthesis process, but may also result in the aggregation or uneven distribution of heteroatom dopants, limiting the activity of the catalyst. Therefore, it is highly desirable to develop alternative MOFs with ligands containing homogeneously distributed S, N, and P atoms and metal moieties that have proper metal cation-to-cation distances.

Herein, we report a rational design and experimental realization of a new 3-dimensional MOF that consists of phosphine, pyridine, and thiocyanate ligands, providing both TMs and P, N as well as S sources. This new MOF enables the facile preparation of TMP and TMS nanoparticles embedded in heteroatom-doped carbon matrix (TMP/C and TMS/C) without the need of the post-synthetic phosphorization or sulfurization. Using this MOF, we have successfully synthesized an electrocatalyst featuring blended NiP/NiFeP nanoparticles encapsulated by (N, P)-codoped carbon (NiP/NiFeP/C). The obtained NiP/NiFeP/C catalyst exhibited excellent activities for both HER and OER. When NiP/NiFeP/C was used as both the anode and the cathode in a two-electrode alkaline water electrolyzer, low cell voltages of 1.53 V and 1.68 V were achieved to reach stable current densities of 10 and 100 mA cm^{-2}, respectively. Furthermore, using the same strategy, we have also synthesized mixed $Mo_{0.5}W_{0.5}S_2$ and MoP ultrafine nanoparticles encapsulated in (N, S)-codoped carbon matrix (MoWS/MoP/C), which showed higher activities than both MoS_2 and WS_2 catalysts, revealing the potential of the new MOF approach for facile synthesis of other TMP/TMS nanoparticles encapsulated in doped carbon matrix.

Experimental section

Materials: Nickel chloride (NiCl$_2$, 99%), 1,3-dichloropropane (99%), glyoxal (40% solution), potassium hydroxide (KOH, 99%), potassium thiocyanate (99.7%), nickel hydroxide, [1,3-Bis(diphenylphosphino)propane (DPPP), nickel chloride (NiCl$_2$), iron (II) chloride (FeCl$_2$), Molybdenum hexacarbonyl (98%), Octadecene (99%), octylamine (70%), Sulfur (99%), Sodium hypophosphite (99%, NaH$_2$PO$_2$), Sodium acetate (99%, NaAc), hydrochloric acid (HCl), ammonium water and methanol were purchased from Sigma-Aldrich Co. Ltd. Nafion solution (5 wt%, D521) and Nafion 117 proton exchange membrane were purchased from Fuel cell store. 1,3-Di(4-pyridyl)propane and 2-(2-(1H-imidazol-2-yl)propyl)-3H-imidazole were synthesized according to the literature reports.[39, 40] (Bu$_3$N)$_3$W(CN)$_8$ and (Bu$_3$N)$_3$Mo(CN)$_8$ were synthesized according to our previous report.[27]

Electrocatalysts synthesis: [NiFeDPPP(1,3-Di(4-pyridyl)propane)$_2$]$_n$: 1,3-Di(4-pyridyl)propane, KOH, DPPP, NiCl$_2$ and FeCl$_2$ were mixed in methanol with a molar ratio of 2:4:1:0.95:0.5. And the mixture was stirred at room temperature. The red-colored mixture turned to transparent red-colored solution and then turned light red, then yellowish-red, then yellowish green and then green slurry. Turquoise solid was obtained after filtrations and washed with methanol and dried in vacuum at 80°C overnight. [Mo$_{0.5}$W$_{0.5}$DPPP(SCN)$_3$]$_n$: (Bu$_3$N)$_3$W(CN)$_8$ and (Bu$_3$N)$_3$Mo(CN)$_8$ were dissolved in methanol, then DPPP and potassium thiocyanate were added. The dark-red precipitation was collected after filtrations and washed with methanol and dried in vacuum at 80°C overnight. The as-synthesized solids were placed in the center of a tube furnace and was anneal for 3 h at various temperatures with a temperature ramping rate of 5 °C min^{-1}.

Synthesis of Ni$_{12}$P$_5$, MoS$_2$, WS$_2$, and RuO$_2$ and IrO$_2$ control samples: Ni$_{12}$P$_5$: Commercial Ni nanoparticles (1.0 g) were dispersed in deionized water (50 mL) to become a black slurry, and then NaH$_2$PO$_2$ and NaAc powders were added to the slurry under stirring with a molar ratio of 1:6:1 (Ni:NaH$_2$PO$_2$:NaAc). The pH level was then adjusted to be 8.0 using 1.0 M KOH and the slurry was further heated to 90 °C for 1 h under N$_2$ atmosphere. The color of the slurry turns darker, and the black product was collected by filtration and dispersed in 5.0 M HCl to remove unreacted Ni and then filtrated and washed with deionized water. *Synthesis of MoS$_2$, WS$_2$, MoP samples*: M(CO)$_6$ (M = Mo, W, 1mmol) was dissolved in octadecene (10 mL), the solution was further heated to 320 °C at 3.3 °C min^{-1} and then was kept at this temperature for 2 h. The black perceptions were washed with ethanol and filtrated to be a sticky solid. S was dissolved in octylamine at 140 °C under nitrogen atmosphere and the solution was

cooled down to room temperature to form a clear red solution. Then, the sticky solid was dissolved in the red solution, and the solution was heated rapidly to 200 °C and hold for 3h under nitrogen atmosphere to obtained MS_x. The sticky solid was placed in the center of a tube furnace and NaH_2PO_2 (molar ratio of 10 to 1) was placed in the upstream of the furnace and the MP can be obtained at 450 °C for 3h under nitrogen flow of 200 sccm. RuO_2 and IrO_2 were synthesized according to the literature.[41, 42] Cyclic voltammetry was performed at the potential region from 0.06 to 0.96 V (vs Ag/AgCl/KCl) with a scan rate of 50 mV s^{-1}. After electrodeposition, the obtained films were annealed at 200°C for 3 h in air. The solution was 0.45 g $RuCl_3$/$IrCl_3$, 2.98 g KCl and 0.01 M HCl. The as-prepared nanoparticles have an average grain size of 500 nm.

Materials characterizations: The structure and phase of the synthesized materials were examined by X-ray diffraction (XRD) (Ultima III, Rigaku, Japan) and Raman spectroscopy (Bruker FT Raman Spectrometer with laser wavelength of 532 nm). The morphology of the films was characterized by a scanning electron microscope (SEM) (Hitachi S-4800, Hitachi, Japan), a transmission electron microscope (TEM) (JEOL 3011, JEOL, Japan), and scanning transmission electron microscope (STEM) (Hitachi HD-2300A, Hitachi, Japan). Elemental compositions were measured by energy-dispersive X-ray spectroscopy (EDX) (Oxford Instruments, UK) and inductively coupled plasma mass spectrometry (ICP-MS, Thermo Scientific XSeries 2 ICPMS, USA). Proton nuclear magnetic resonance (^1H NMR) spectra were collected at 600 MHz on a Bruker model AMX 600 spectrometer. Fourier-transform infrared (FT-IR) spectra were collected on a Nexus spectrometer (Nicolet, USA) using KBr disks. X-ray photoelectron spectroscopy (XPS) was performed on a VG ESCALABMK II spectrometer using an Al K_α (1486.6 eV) photon source.

Electrochemical measurements: 2 mg of catalyst was dissolved in 2 mL ethanol and 100 μL Nafion solution was added. Then the mixture was sonicated for 30 min to form a homogenous mixture. Then 90 μL of the slurry was loaded onto the surface of a glassy carbon electrode (GCE, 0.196 cm^2) and the electrode was dried at room temperature. Electrolyte was purified to remove trace Fe using $Ni(OH)_2$ powder.[43] The electrochemical measurements were performed using a Voltalab PGZ-301 potentiostat/galvanostat (Radiometer Analytical, France), with a platinum foil and an Ag/AgCl electrode used as the counter and reference electrodes, respectively. The HER and OER characterization were carried out on a glassy carbon rotating disk electrode. For preparing water splitting electrodes, 1.5 mm

thick nickel foam (>99.5%, 1.5 mm, MTI Corporation, USA) was compressed to ~1 mm using a

hydraulic press, which helped increase the adhesion of the catalysts and to define the geometric area. The

as-prepared catalysts and RuO_2 and IrO_2 are dropped on the surface of Ni foam and dried in Air. The

loading amount of catalysts is 0.168 mg cm^{-2}. The potentials were displayed versus reversible hydrogen

electrode (RHE) by: $E_{(RHE)} = E_{(Ag/AgCl)} + 0.197 + 0.0591 \times pH$. All the linear sweep voltammetry

measurements were carried out at a scan rate of 1 mV·s^{-1}. All of the electrochemical measurements were

not iR-compensated. The stability test was performed using the controlled current electrolysis method.

The H_2 and O_2 evolution was conducted under potentiostatic mode. Gaseous products from the outlet of

the electrode compartment were vented directly into the gas-sampling loop of the gas chromatograph

(GC, InficonMicro 3000 GC), with a GC run initiated every 25 min. The gas concentration was averaged

over three measurements. Faradaic efficiency was calculated according to that 96485 C of electrons can

generate 0.5 mol of H_2 and 0.25 mol of O_2. Electrochemical impedance spectroscopy (EIS) measurements

were carried out at 1.23 V (vs. RHE) in the frequency range of 100 kHz to 0.1 Hz with a single modulated

AC potential of 5 mV. Turnover frequency was calculated according to literature report, and the number

of metal ions was determined from ICP analysis.[25] Briefly, TOF = numbers of O_2 turnovers/numbers of

metal ions, and the numbers of O_2 turnovers = $(j \ (@1.51 \ V_{RHE}) \times A \times atoms)/96485n = 3.062 \times 10^{17} \ O_2$

s^{-1} per Acm^{-2}, where $A = 0.1963$ cm^2 (5 mm diameter), $atoms = 6.02 \times 10^{23}$ mol^{-1}, and n = 4.

Results and discussion

Owing to the unpopulated metal $3d$ electrons in both e_g and t_{2g} orbitals, TM ions (Ni, Co, Fe, W,

Mo, etc) usually can produce up to six (for Co, Ni, Fe, etc) or eight (for W, Mo, etc) coordination

polyhedrons.[27] The P and N atoms in phosphine- and pyridine-based (or imidazole-based) ligands,

respectively, can donate one electron from their sp^2 orbitals to the unoccupied orbitals of TMs through σ

bonds.[27] Based on this, a class of $3d$ TM-organic open framework (**Fig. 1a**) was designed and then

synthesized at room temperature by coordinating Ni and Fe ions with 1,3-

bis(diphenylphosphino)propane, 1,3-bis(4-pyridyl)propane (or 2-(2-(1H-imidazol-2-yl)propyl)-3H-

imidazole (the synthesis and proton nuclear magnetic resonance characterizations are provided in the

supporting information and **Fig. S1**). The formula of the obtained Ni/Fe-MOF is (Ni/Fe)$N_2P_2C_{42}H_{37}$. **Fig.**

1a presents a single unit cell and **Fig. 1b** shows 8 unit cells (4 in a-axial and 4 in b-axial) of the Ni/Fe-

MOF. Each Ni/Fe cation chelate–bridges two P from the 1,3-bis(diphenylphosphino)propane and two N from 1,3-bis(4-pyridyl)propane, while adjacent TM atoms are separated by at least two propanebenzene rings. Thus, the issue of insufficient distance between metal atoms, as found in imidazole-based zeolitic imidazolate frameworks (ZIFs), is mitigated. Compared to ZIFs, each Ni/Fe cation in the Ni/Fe-MOF is also bonded with two additional P atoms besides the same amount of N atoms by using 2-(2-(1H-imidazol-2-yl)propyl)-3H-imidazole as a linker molecule, which enables us to avoid post-synthetic processing for further phosphorization. X-ray diffraction (XRD) analysis (**Fig. 1c**) reveals a triclinic space group $P1$ (with lattice parameters of a = 21.00631 Å, b = 12.96327 Å, c = 17.19418 Å) for the obtained Ni/Fe-MOF. The experimental and simulated XRD patterns match closely (**Fig. 1c**), indicating high phase purity for the synthesized samples. The corresponding Fourier-transform infrared spectroscopy (FTIR, **Fig. S2**) pattern shows two characteristic peaks located at 1020 and 1613 cm^{-1}, which can be ascribed to the in-plane bending and the stretching vibrations of pyridine rings, respectively.[31] The peak at 1426 cm^{-1} can be ascribed to the stretching and asymmetrical deformation vibrations of aromatic phosphines (P-Ar).[32] The Ni/Fe-MOF was then treated under 50 sccm Ar flow at 600, 700, and 800 °C with a heating rate of 5 °C min^{-1}. The corresponding XRD patterns (**Fig. 1d**) suggest that the resultant samples are amorphous at 600 °C and crystallized into cubic-structured Ni (space group: $Fm3m$, No. 225) at 700 °C (Ni/C). Notably, the sample obtained at 800 °C shows the main tetragonal-structured $Ni_{12}P_5$ phase (space group of $I4/m$, No. 87) with minor hexagonal-structured NiFeP phase (space group of $P62m$, No. 189) and is denoted as NiP/NiFeP/C. Further examination shows that the peak positions of the sample NiP/NiFeP/C obtained at 800 °C shift toward smaller angles by 0.1° to 0.15°, suggesting Fe doping into $Ni_{12}P_5$ (**Fig. S3**).[8] Compared to traditional methods of synthesizing TM phosphides, which usually have residues of P_2O_5 or red phosphorus,[2-5] our approach is easy and free of hazardous P residues, enabling fast sample preparation. In addition, the supporting carbon matrix, which is beneficial for the electron transportation, can also be produced at the same time using our facile method.

The obtained NiP/NiFeP/C sample consists of nanoparticles (NPs, **Fig. 2a**, labeled with white arrows) with diameters of 40 - 200 nm dispersed in the carbon matrix. Interestingly, some carbon nanostructures are seen in the form of nanofibers with an average diameter of 40 nm and an average length of 2 μm (**Fig. S4**). Further transmission electron microscopy (TEM) characterization shows ~50 nm nanoparticles

with a ~5 nm amorphous shell embedded in the carbon matrix (**Fig. S5**). To further verify the composition, elemental distribution measurements were carried out using scanning transmission electron microscopy (STEM) equipped with energy dispersive X-ray (EDX) elemental mapping and EDX linear scanning (**Fig. 2b to 2j**). As indicated, Ni and Fe are homogeneously distributed in the NPs, while N, P and O are also distributed in the carbon matrix, indicating N-, P-, and O-doping of the carbon matrix. The STEM-EDX linear scanning further reveals that the NP is composed of Ni and Fe phosphides, and a thin $NiFeO_x$ shell on its surface. The presence of O indicates slight oxidation of the phosphides, which may arise from the oxidation of phosphide in the ambient air or the O-containing small molecules (*i.e.* water and methanol as solvent for the synthesis) during the pyrolysis process.

X-ray photoelectron spectroscopy (XPS) measurements were also carried out (**Fig. S6**). The peaks at 855.4 and 873.3 eV for Ni 2p are assigned to Ni $2p_{3/2}$ and Ni $2p_{1/2}$, respectively,[1] which can be fitted with three oxidation states of Ni^{0+}, Ni^{2+}, and Ni^{3+}, located at 855.1, 856.4, and 858.3 eV, respectively.[44] The Fe 2p peaks are comprised of both Fe^{3+} and Fe^{4+}.[19] Fe^{4+}, which may arise from the surface oxidation,[1] can also contribute to the high OER performance by creating a higher degree of metal-oxygen covalency, thus facilitating the interactions between adjacent adsorbed oxygen atoms forming oxygen molecules.[19] The P 2p peaks at 129.8 and 130.7 eV correspond to P $2p_{3/2}$ and P $2p_{1/2}$ orbitals, respectively, which are characteristic of metal phosphides, and the peaks located at 134.4 and 133.1 can be ascribed to P-O and P-C.[27] The spectrum also contains strong P-O peak at 134.3 eV, which is consistent with the STEM-EDX observations. The C 1s peak centered at approximately 285.7 eV is assigned to sp^2 hybridized graphitic carbon in C=N bonds, which is common for N-doped carbon.[27] The peak positioned at 284.2 eV can be ascribed to graphitic carbon,[27] while the peak positioned at 287.0 eV corresponds to oxidized carbon, which has better aqueous wetting properties and facilitates electrolyte uptake, hence favoring the improvement of the activity for water splitting reactions. The N 1s peaks around 398.7 eV and 399.5 eV are ascribed to pyridine and pyrrolic nitrogen, respectively,[27] which are believed to be the active sites for both HER and OER.[27] To further verify the N and P doping in the carbon matrix, Raman measurement was also conducted. As indicated in **Fig. S7**, Raman spectrum contains two characteristic peaks positioned at 1349 and 1586 cm^{-1}, corresponding to the D and G bands of N-doped carbon, respectively.[26] The corresponding intensity ratio (I_D/I_G), which is correlated to the quantity of defects, is estimated to be 1.31, indicating successful doping of N and P.[26] N- and P-doping

lead to positively charged carbons bonded with more electronegative nitrogen and phosphorus due to the difference of electronegativity, and as a result, the adsorption of adsorbates can be improved.[27] Moreover, nitrogen and phosphorus can exchange electrons with the attached NPs, even further improving the catalytic activity.[27] The elemental contents of the NiP/NiFeP/C sample were determined by XPS and inductively coupled plasma mass spectrometry to be 62.3% C, 20.7% Ni, 0.8% Fe, 7.3% N, 5.8% P, and 3.1% O.

The electrocatalytic performance of NiP/NiFeP/C was firstly evaluated for HER in acidic solution (**Fig. 3**). Pt was served as a counter electrode, which was separated with working electrode through Nafion 117 proton exchange membrane in a H-cell to prevent re-deposition of Pt from the anode to the working electrode. Pt/C (commercial Pt/C, 20% Pt, mass loading of 0.168 mg cm^{-2}) and NiFe-LDH (mass loading of 0.168 mg cm^{-2}) were compared as references. Pt/C shows an onset potential of 0 mV (vs. RHE) and achieves a stable current density of -10 mA cm^{-2} at a potential of -49 mV (vs. RHE) with a Tafel slope of 30 mV dec^{-1}, in good accordance with literature reports.[16-35] In contrast, NiFe-LDH exhibits much inferior activity, which achieves a current density of -4 mA cm^{-2} at -300 mV (vs. RHE) with a Tafel slope of 112 mV dec^{-1}. For Ni/Fe-MOF derived electrocatalysts (mass loading of 0.168 mg cm^{-2}), pyrolysis temperature was found to affect the catalytic properties. The amorphous sample obtained through pyrolysis at 600 °C shows negligible HER activity, whereas the Ni/C sample obtained by pyrolysis at 700 °C displays improved HER catalytic activity, which achieves -8 mA cm^{-2} at -280 mV (vs. RHE), better than NiFe-LDH. The valence state of Ni in the Ni/C sample has lower Gibbs free energy for H* absorption/desorption ($|\Delta G_{H*}|$) than in NiFe-LDH, thus enabling higher HER activities than in NiFe-LDH.[23] More remarkably, the NiP/NiFeP/C sample reaches a current density of -10 mA cm^{-2} at -87 mV (vs. RHE), which is only 38 mV higher than that of Pt/C. The corresponding Tafel slope is 38 mV dec^{-1}, which is also comparable to that of Pt/C, indicating the rate limiting process of HER is the Heyrovsky-Tafel reaction rather than the Volmer-Heyrovsky reaction due to the stronger H* absorption of metal phosphides.[8] Moreover, it exhibits the same onset potential of 0 mV (vs. RHE) as Pt/C, further suggesting the superior electrocatalytic activity of the NiP/NiFeP/C, which is also comparable to the most active TM phosphides, chalcogenides, and phosphosulphides with a similar loading amount and the same glass carbon substrate reported in literatures (**Table S1**). To gain more insights into the mechanism, Ni$_{12}$P$_5$ was mixed with mesoporous carbon (NiP-mC) and a sample was obtained through the same

precursor process but without Fe addition (NiP/C) as a control. NiP-mC achieves −10 mA cm^{-2} at a potential of −175 mV (vs. RHE), with the corresponding Tafel slope is 72 mV dec^{-1}, while the NiP/C sample can deliver the same current density at −131 mV (vs. RHE), with a corresponding Tafel slope of 61 mV dec^{-1}. NiP/C, therefore, has better catalytic activity than NiP-mC, suggesting that the more electrochemically active metal phosphide/carbon interfaces of NiP/C were formed by the *in-situ* transformation from MOF structure. More importantly, NiP/NiFeP/C exhibits even superior catalytic activity to NiP/C, indicating that the presence of minor NiFeP secondary components further favors the activity. Electrochemical impedance spectroscopy (EIS) was also carried out to evaluate the charge transfer during hydrogen evolution (**Fig. 3c**). Circuit model fitting analysis showed that the impedance data can be modeled using a modified Randles circuit consisting of a series resistance (R_s), constant phase element (*CPE*), charge transfer resistance (R_{ct}), and modified mass-transport impedance element (M_a).[27] The impedance data and associated Randles equivalent circuit are shown in **Fig. 3c**. The radius of the semi-arc corresponds to *CPE* and R_{ct}. The smaller R_{ct} of 6.8 Ω for NiP/C than NiP-mC (9.9 Ω) indicates that the interfaces of the conductive carbon matrix and the NiP/NiFeP NPs facilitate the charge transfer and thereby improve the electrocatalytic activity. Notably, the NiP/NiFeP/C sample shows the smallest R_{ct} of 2.5 Ω, compared to NiP/C and NiP-mC, suggesting that a little amount of NiFeP can further facilitate the charge transfer and the catalytic activity. The results show that the superior activity of NiP/NiFeP/C can be ascribed to the synergistic effect of $Ni_{12}P_5$, NiFeP, and carbon matrix. Long-term stability is crucial for the electrocatalyst to be used practically. Herein, the NiP/NiFeP/C sample also manifests superior stability over 98% potential retaining when performed galvanostatically for 20 h (**Fig. 3d** inserted plot), and the linear sweep voltammetry also only shows only slight degradation after 20 h stability test, indicating excellent stability of NiP/NiFeP/C (**Fig. 3d**).

To further study the intrinsic catalytic activities, the geometric current densities are normalized by the relative electrochemical surface areas (ECSA). The double-layer capacitance (C_{dl}), proportional to the electrochemically active surface area and derived from the cyclic voltammetry measurements, is one of the descriptors for determining the ECSA.[27] Although the electrochemical capacitances of the carbon matrix contribute to the C_{dl} and thereby affect the ECSA, the normalization of the geometric current densities by the estimated ECSA can still reflect the intrinsic activities. NiP-mC shows the highest C_{dl}, followed by NiP/NiFeP/C and NiP/C (**Fig. 3e**). The higher C_{dl} indicates more contact between active

sites and electrolyte for electron transfer.[27] The higher C_{dl} of NiP-mC than that of NiP/NiFeP/C may be caused by the higher electrochemical surface area of mesoporous carbon, which is electrochemically active for supercapacitors but inert for HER. The normalized current densities, which stand for the number of active sites per relative surface area, are given in **Fig. 3f**. NiP/NiFeP/C is the most active compared to NiP/C and NiP-mC, even though the ECSA contribution of carbon is also counted. It, therefore, is rational to believe that the intrinsic activity of NiP/NiFeP/C will be higher without counting the carbon. In addition, the exchange current densities are then normalized by the relative surface areas. The normalized exchange current densities ($J_{0, normalized}$), which stands for the number of active sites per relative surface area, are given in **Table S2**. The NiP/NiFeP/C shows the highest $J_{0, normalized}$, compared to NiP/C and NiP-mC samples, and therefore, exposes much more active sites, enabling the improvement of HER catalytic activity. The high intrinsic activity of NiP/NiFeP/C arises from its unique architecture, which results in the good interfaces facilitating the charge transfer and the synergistic effect of $Ni_{12}P_5$ and NiFeP in the NPs. The incorporation of Fe facilitates the HER activities. We also measured the HER electrocatalytic performance of NiP/NiFeP/C in alkaline solution with Pt as counter electrode. NiP/NiFeP/C exhibits −138 mV (vs. RHE) to achieve −10 mA cm^{-2}. The corresponding Tafel slope is 68 mV dec^{-1}. (**Fig. S8**). Moreover, the NiP/NiFeP/C electrocatalyst maintains over 90% of its current and/or potential retention after 20 h of stability testing. The results show that NiP/NiFeP/C also has favorable HER electrocatalytic activity and stability in alkaline electrolyte (**Table S3**).

The NiP/NiFeP/C sample was then tested for OER in alkaline solution. RuO_2 and NiFe-LDH (mass loading of 0.168 mg cm^{-2}) were added for comparison. RuO_2 shows (**Fig. 4a**) an onset potential of 1.45 V (vs. RHE) and achieves a stable current density of 10 mA cm^{-2} at a potential of 1.55 V (vs. RHE) with a Tafel slope of 81 mV dec^{-1}, in good accordance with literature reports.[1] NiFe-LDH shows an onset potential of 1.42 V (vs. RHE) and achieves a stable current density of 10 mA cm^{-2} at a potential of 1.53 V (vs. RHE) with a Tafel slope of 62 mV dec^{-1}, consistent with literature reports.[6] All of the Ni-based samples show current bump/peak during positive scanning (**Fig. S9**, labeled with a red arrow), which is contributed by the redox feature of Ni, *i.e.* current density from the oxidation of low valence state of Ni atoms, while the reverse scan shows a cathodic peak, correlated to the reduction of NiOOH.[50] The Faradaic current from Ni^{2+} oxidation does not contribute to the water oxidation, so the reverse scan (**Fig. S9**, labeled with a black arrow) should well represent the OER activity of the sample. The NiP/NiFeP/C

sample exhibits better performance than RuO_2, NiFe-LDH, and the samples obtained at low pyrolysis temperatures. It is worth mentioning that given the carbon content of 62.3 %, the actual loading amount of active NiP/NiFeP is much lower. NiP/NiFeP/C achieves 10 mA cm^{-2} at a potential of 1.48 V (vs. RHE) with a corresponding Tafel slope of 58 mV dec^{-1} (**Fig. 4b**). In contrast, the corresponding MOF pyrolyzed at 600 °C reaches a current density of 5 mA cm^{-2} at 1.69 V (vs. RHE) with a corresponding Tafel slope of 116 mV dec^{-1}; the sample Ni/C obtained through the corresponding MOF pyrolyzed at 700 °C shows a potential of 1.59 V (vs. RHE) at a current density of 10 mA cm^{-2} with a corresponding Tafel slope of 70 mV dec^{-1} (**Fig. 4b**). The OER activities of the NiP/C and NiP-mC were also compared. NiP/C reaches a current density of 10 mA cm^{-2} at 1.50 V (vs. RHE) with a corresponding Tafel slope of 60 mV dec^{-1}, while the NiP-mC needs 1.57 V (vs. RHE) to deliver the same current density. NiP/C, therefore, shows the better OER catalytic activity than NiP-mC, due to the good interfaces between $Ni_{12}P_5$ and carbon matrix. More remarkably, given the synergistic effect of $Ni_{12}P_5$ and NiFeP in the NPs, NiP/NiFeP/C has further enhanced OER catalytic activity, further demonstrating that the incorporation of Fe will further boost the electrocatalytic activities both on HER and OER. Then, the mass activity (MA), obtained by the normalization of the geometric current density to the oxide mass loading, was also calculated and compared to other reported OER electrocatalysts (**Fig. 4c**). The NiP/NiFeP/C catalyst delivers much better MA than NiFe-LDH and some other OER electrocatalysts. Specifically, the catalyst exhibits a MA of 78.3 A g$^{-1}_{cat}$, which is ~1.3 times higher than that of NiFe-LDH.[6] EIS measurements exhibit that the NiP/NiFeP/C has the smallest R_{ct} (**Fig. S10**), suggesting the superior charge transfer, which is in good agreement with the electrocatalytic activity analysis. Moreover, the turnover frequency (TOF) was estimated by normalizing the rate of O_2 generation to the total number of metal ions.[25] The TOF of NiP/NiFeP/C at 1.51 V (vs. RHE) was estimated to be 0.133 s^{-1} (See Supporting Information for details), indicating the outstanding OER activity of NiP/NiFeP/C, which is higher than that of the majority of the most active OER catalysts (**Table S4**). For example, IrO_2 delivers a TOF of 0.050 s^{-1} at 1.53 V (vs. RHE);[51] $NiCeO_x$–Au delivers a TOF of 0.080 s^{-1} at 1.51 V (vs. RHE);[25] NiFe-LDH reaches a TOF of 0.036 s^{-1} at 1.51 V (vs. RHE) and 0.075 s^{-1} at 1.65 V (vs. RHE).[6] Notably, the estimation of TOF for NiP/NiFeP/C is based on the presumption that all of the metal cations are involved in the water oxidation reactions, although some may not participate in the reactions. If only the active sites on the surface are counted, the actual TOF of NiP/NiFeP/C would be even higher. The stability of NiP/NiFeP/C

was also evaluated in an alkaline electrolyte at a constant potential of 1.52 V (vs. RHE) (**Fig. 4e**). The

NiP/NiFeP/C maintains a stable current density with almost 98% retention after 20 h of stability testing.

For pristine TM phosphides, surface oxidation leads to the formation of TM hydroxides and phosphates;

the dissolution of the phosphates results in the leaching of P.[2-5] Consequently, the OER performance

will decrease during the long-term operation. For our material of NiP/NiFeP/C, the thin amorphous shell

(indicated in **Fig. 2j**) and the carbon matrix can effectively mitigate the activity decay during the long-

term operation in alkaline solution due to P leaching. After OER durability test, NiP/NiFeP/C still

maintains the same morphology (**Fig. S11**). The STEM-EDX of NiP/NiFeP/C after stability test shows

that the oxygen content in the composite increases (**Fig. S12**). The increase of O content in the carbon is

consistent with the experimental observation of the enhancement in hydrophilicity of the sample after

stability test. Further XRD measurement (**Fig. S13**) confirms the presence of $NiFe(OOH)_x$, in good

agreement with the STEM-EDX result, implying that the amorphous $NiFeO_x$ shell of the NiP/NiFeP/C

sample can be converted to the $NiFe(OOH)_x$ shell,[10] which can prevent leaching of the phosphide core.

The XPS measurement (**Fig. S14**) shows that the NiP/NiFeP/C sample only has slight increase of the P-

O peak intensity after the stability test, indicating negligible P leaching during long-term test, and thus

further confirming the good stability of NiP/NiFeP/C. Therefore, the double protection of the

$NiFe(OOH)_x$ shell and the carbon matrix confer NiP/NiFeP/C the outstanding stability.

Both electrochemical water splitting and CO_2 reduction require OER electrocatalysts, and

electrochemical water splitting prefers alkaline solutions, while CO_2 reduction prefers neutral aqueous

solutions due to the difference in the solubility of active intermediates.[52] The OER performance of

NiP/NiFeP/C, therefore, was also evaluated in a neutral pH aqueous electrolyte (**Fig. 4f**). The

NiP/NiFeP/C sample manifests a potential of 1.55 V (vs. RHE) at 1 mA cm^{-2} and a corresponding Tafel

slope of 132.8 mV dec^{-1}, which is superior to that of RuO_2 (potential at 1.0 mA cm^{-2}: 1.58 V (vs. RHE)

and Tafel slope: 199.3 mV dec^{-1}). Importantly, the NiP/NiFeP/C is among the most active OER

electrocatalysts in neutral solution. For instance, $CoO_2/CoSe_2$-Ti[7] and CoP@Co-Bi-Pi/Ti[9] exhibit 1.74

and 1.65 V (vs. RHE), respectively, at 1.0 mA cm^{-2} in neutral solutions. Therefore, NiP/NiFeP/C is a

good OER electrocatalyst in both alkaline and neutral solutions.

Both excellent HER and OER activities could enable NiP/NiFeP/C to be an efficient bifunctional

catalyst for overall water splitting. To validate this, a two-electrode water-splitting device using

NiP/NiFeP/C coated on Ni foam (NiP/NiFeP/C-NiF) as both anode and cathode was assembled and tested in 1.0 M KOH. The half-cell reactions were firstly examined. NiP/NiFeP/C-NiF reaches the cathodic current density (**Fig. 5a**) of 10 mA cm^{-2} and 100 mA cm^{-2} at potentials of -75 and -179 mV, respectively, reflecting the good HER catalytic activity. NiP/NiFeP/C-NiF requires 1.40 and 1.46 V (vs. RHE) to deliver the anodic current density of 10 and 100 mA cm^{-2}, respectively (**Fig. 5a**), also manifesting the good OER catalytic activity. When combined together, the two-electrode water-splitting device achieves a current density of 10 and 100 mA cm^{-2} at a potential of 1.53 V and 1.68 V in alkaline solution (**Fig. 5b**), superior to the benchmark of noble metal combination, $RuO_2(+)\|Pt(-)$ and comparable to the most highly active bifunctional electrocatalysts reported in literature (**Fig. 5c**). Stability test was further undertaken for the full water-splitting configuration at 100 mA cm^{-2}. The potential was observed to be stable for over 20 h under continuous operation (**Fig. 5d**). Gas chromatography measurement confirms a high faradic efficiency of 99.8% and generated H_2 and O_2 concentrations at a predicted ratio of 2:1 (**Fig. S15**). The result indicates that NiP/NiFeP/C-NiF is a good and efficient bifunctional electrocatalyst for overall water splitting.

To demonstrate the versatility of the new MOF for producing heteroatom-doped carbon encapsulated non-3d TM phosphide or sulfide nanoparticles for HER or OER, 4d-Mo and 5d-W based phosphide/sulfide have also been synthesized. The XRD pattern (**Fig. S16**) of the synthesized Mo, W-MOF indicates a triclinic space group $P1$ (with lattice parameters of $a = 10.83525$ Å, $b = 11.24025$ Å, $c = 16.45438$ Å), and the corresponding XRD pattern (**Fig. S17a**) of the sample obtained by pyrolysis of Mo, W-MOF at 800 °C suggests the main trigonal-structured $Mo_{0.5}W_{0.5}S_2$ phase (space group of $P3m1$, No. 156) with a small portion of the hexagonal-structured MoP phase (space group of $P62m$, No. 187). The structure of $Mo_{0.5}W_{0.5}S_2$ (**Fig. S17**) is similar to its counterpart, 2H-MoS_2, but has greatly expanded interlayer spacing (~ 12.6 Å), which means the $Mo_{0.5}W_{0.5}S_2$ can be treated as 2-dimensional Janus MoS_2/WS_2 layers.[62, 63] The XRD measurement also indicates that $Mo_{0.5}W_{0.5}S_2$ has the highest edge-to-plane ratio among all of the reported 2H-WS_2 or MoS_2 nanostructures, and the electrochemically inert (001) plane is remarkably inhabited. The obtained sample (denoted as MoWS/MoP/C) has a particle diameter of 100 to 600 nm, composed of small nanoparticles with diameter of ~ 6 nm homogenously dispersed in a carbon shell (**Fig. S18**).

The electrochemical activity of MoWS/MoP/C was also evaluated for HER in acidic solution (**Fig. S19**). Apart from Pt/C, $(NH_4)_2Mo_3S_{13} \cdot nH_2O$ was also compared as reference, because $(NH_4)_2Mo_3S_{13} \cdot nH_2O$, which was also synthesized using a straightforward wet-chemistry method at room temperature (**Fig. S20**),[64] was reported recently as a robust electrocatalyst for HER. MoWS/MoP/C achieves -10 mA cm^{-2} at -149 mV (vs. RHE), and the corresponding Tafel slope is 45 mV dec^{-1}. In contrast, $(NH_4)_2Mo_3S_{13} \cdot nH_2O$ delivers a current density of -10 mA cm^{-2} at -250 mV (vs. RHE) with a Tafel slope of 61 mV dec^{-1}, which is better than that of MoS_2, but the activity is still much inferior to that of MoWS/MoP/C, which may be caused by the still poor electron collection properties of $(NH_4)_2Mo_3S_{13} \cdot nH_2O$.[64] The results well demonstrate that our proposed approach is feasible and easy to synthesize 3d to 5d TM phosphide or sulfide NPs encapsulated in heteroatom-doped carbon matrix for highly efficient water splitting.

Conclusions

We have designed and synthesized new MOFs that enable facile, one-step preparation of 3d to 5d TM phosphide or sulfide nanoparticles $e.g.,$ $Ni_{12}P_5$/NiFeP NPs (NiP/NiFeP/C) and $Mo_{0.5}W_{0.5}S_2$/MoP ultrafine NPs (MoWS/MoP/C), encapsulated in heteroatom-doped carbon matrix. The NiP/NiFeP/C electrocatalyst shows competitive HER catalytic activity to the best HER electrocatalysts reported in literature and higher OER activity than noble metal oxide catalysts, such as RuO_2. A two-electrode water-splitting device using bifunctional NiP/NiFeP/C catalysts achieves 10 mA cm^{-2} at a cell voltage of 1.53 V and 100 mA cm^{-2} at 1.68 V with excellent stability for overall water splitting at 100 mA cm^{-2} for over 20 h. Moreover, the MoWS/MoP/C catalyst exhibits better HER activity than MoS_2 and $(NH_4)_2Mo_3S_{13} \cdot nH_2O$ reported in literature. Our results demonstrate the potential of the new MOFs for facile synthesis of highly efficient TM electrocatalysts.

Acknowledgement

References

[1] B. Weng, F. Xu, C. Wang, W. Meng, C. R. Grice and Y. Yan, *Energy Environ. Sci.,* 2017, **10**, 121.

[2] F. Hu, S. Zhu, S. Chen, Y. Li, L. Ma, T. Wu, Y. Zhang, C. Wang, C. Liu, X. Yang, L. Song, X. Yang and Y. Xiong, *Adv. Mater.*, 2017, **29**, 1606570.

[3] W. J. Yin, B. Weng, J. Ge, Q. Sun, Z. Li and Y. Yan, *Energy Environ. Sci.*, 2019,12, 442.

[4] X. Han, X. Wu, Y. Deng, J. Liu, J. Lu, C. Zhong and W. Hu, *Adv. Energy Mater.*, 2018, 1800935.

[5] L. A. Stern, L. Feng, F. Song and X. Hu, *Energy Environ. Sci.*, 2015, **8**, 2347.

[6] X. Lu and C. Zhao, *Nat. Commun.*, 2015, **6**, 6616.

[7] X. Liu, H. Zheng, Z. Sun, A. Han and P. Du, *ACS Catal.*, 2015, **5**, 1530.

[8] Z. Zhang, Y. Qin, M. Dou, J. Ji and F. Wang, *Nano Energy*, 2016, **30**, 426.

[9] W. Wang, D. Liu, S. Hao, F. Qu, Y. Ma, G. Du, A. M. Asiri, Y. Yao and X. Sun, *Inorg. Chem.*, 2017, **56**, 3131.

[10] Z. M. Peng and H. Yang, *J. Am. Chem. Soc.*, 2009, **131**, 7542.

[11] Y. Y. Liang, Y. G. Li, H. L. Wang, J. G. Zhou, J. Wang, T. Regier and H. J. Dai, *Nat. Mater.*, 2011, **10**, 780.

[12] E. J. Popczun, C. G. Read, C. W. Roske, N. S. Lewis and R. E. Schaak, *Angew. Chem. Int. Ed.*, 2014, **53**, 5427.

[13] M. W. Kanan and D. G. Nocera, *Science,* 2008, **321**, 1072.

[14] M. Cabán-Acevedo, M. L. Stone, J. R. Schmidt, J. G. Thomas, Q. Ding, H. C. Chang, M. L. Tsai, J. H. He and S. Jin, *Nat mat.,* 2005, **14**, 1245.

[15] X. Yang, A. Y. Lu, Y. Zhu, M. N. Hedhili, S. Min, K. W. Huang, Y. Han, L and J. Li, *Nano Energy,* 2015, **15**, 634.

[16] C. W. Tung, Y. Y. Hsu, Y. P. Shen, Y. Zheng, T. S. Chan, H. S. Sheu, Y. C. Cheng and H. M. Chen, *Nat. Commun.*, 2015, **6**, 8106.

[17] H. W. Liang, S. Bruller, R. Dong, J. Zhang, X. Feng and K. Muller, *Nat. Commun.*, 2015, **6**, 7992.

[18] P. Chen, K. Xu, Z. Fang, Y. Tong, J. Wu, X. Lu, X. Peng, H. Ding, C. Wu and Y. Xie, *Angew. Chem. Int. Ed.*, 2015, **54**, 14710.

[19] S. Yagi, I. Yamada, H. Tsukasaki, A. Seno, M. Murakami, H. Fujii, H. Chen, N. Umezawa, H. Abe, N. Nishiyama and S. Mori, *Nat. Commun.*, 2015, **6**, 8249.

[20] G. Cai, W. Zhang, L. Jiao, S. H. Yu and H. L. Jiang, *Chem.*, 2017, **2**, 791.

[21] J. Luo, J. H. Im, M. T. Mayer, M. Schreier, M. K. Nazeeruddin, N. G. Park, D. T. Tilley, H. J. Fan and M. Grätzel, *Science,* 2014, **345**, 1593.

[22] S. Jin, *ACS Energy Lett.*, 2017, **2**, 1937.

[23] H. Sun, Y. Lian, C. Yang, L. Xiong, P. Qi, Q. Mu, X. Zhao, J. Guo, Z. Deng and Y. Peng, *Energy Environ. Sci.*, 2018, **11**, 2363.

[24] H. Wang, Z. Lu, S. XU, D. Kong, J. J. Cha, G. Zheng, P. C. Hsu, K. Yan, D. Bradshaw, F. B. Prinz and Y. Cui, *PNAS.,* 2013, **110**, 19701.

[25] J. W. Desmond Ng, M. García-Melchor, M. Bajdich, P. Chakthranont, C. Kirk, A. Vojvodic and T. F. Jaramillo, *Nature Energy,* 2016, **1**, 16053.

[26] K. Qu, Y. Zheng, X. Zhang, K. Davey, S. Dai and S. Z. Qiao, *ACS Nano,* 2017, **11**, 7293.

[27] B. Weng, C. R. Grice, W. Meng, L. Guan, F. Xu, Y. Yu, C. Wang, D. Zhao and Y. Yan, *ACS Energy Lett.*, 2018, **3**, 1434.

[28] R. Wang, X. Y. Dong, J. Du, J. Y. Zhao and S.Z. Qiao, *Adv. Mater.*, 2018, **30**, 1703711.

[29] M. Zhang, Q. Dai, H. Zheng, M. Chen and L. Dai, *Adv. Mater.*, 2018, 1705431.

[30] B. Weng, W. Wei, Yiliguma, H. Wu, A. M. Alenizi and G. Zheng, *J. Mater. Chem. A,* 2016, **4**, 15353.

[31] T. P. Gerasimova and S. A. Katsyuba, *Dalton Trans.*, 2013, **42**, 1787.

[32] R. Scaffaro, L. Botta, G. L. Re, R. Bertani, R. Milani and A. Sassic, *J. Mater. Chem.*, 2011, **21**, 3849.

[33] N. H. Attanayake, A. C. Thenuwara, A. Patra, Y. V. Aulin, T. M. Tran, H. Chakraborty, E. Borguet, M. L. Klein, J. P. Perdew and D. R. Strongin, *ACS Energy Lett.*, 2018, **3**, 7.

[34] J. Miao, F. X. Xiao, H. B. Yang, S. Y. Khoo, J. Chen, Z. Fan, Y. Y. Hsu, H. M. Chen, H. Zhang and B. Liu, *Sci. Adv.*, 2015, **1**, e1500259.

[35] M. R. Gao, M. K. Y. Chan and Y. Sun, *Nat. Commun.*, 2015, **6**, 7493.

[36] H. Schäfer, K. Kuepper, J. Koppe, P. Selter, M. Steinhart, M. R. Hansen, and D. Daum, *ACS Catal.*, 2018, **8**, 10914.

[37] H. Schäfer, and M. Chatenet, *ACS Energy Lett.*, 2018, **3,** 574.

[38] H. Schäfer, S. Sadaf, L. Walder, K. Kuepper, S. Dinklage, J. Wollschläger, L. Schneider, M. Steinhart, J. Hardege, and D. Daum, *Energy Environ Sci.* 2015, **8**, 2685.

[39] B. F. Fieselmann, D. N. Hendrickson and G. D. Stucky, *Inorg. Chem.*, 1978, **17**, 2078.

[40] Z. Y. Fu, S. M. Hu, J. C. Dao, J. J. Zjamg and X. T. Wu, *Eur. J. Inorg. Chem.* 2003, 2670.

[41] C. C. L. McCrory, S. Jung, I. M. Ferrer, S. M. Chatman, J. C. Peters and T. F. Jaramillo, *J. Am. Chem. Soc.* 2015, **137**, 4347.

[42] E. Tsuji, A. K. Imanishi, I. Fukui and Y. Nakato, *Electrochim. Acta* 2011, **56**, 2009.

[43] L. Trotochaud, S. L. Young, J. K. Ranney and S. W. Boettcher, *J. Am. Chem. Soc.* 2014**, 136**, 6744.

[44] P. F. Liu, X. Li, S. Yang, M. Y. Zu, P. Liu, B. Zhang, L. R. Zheng, H. Zhao and H. G. Yang, *ACS Energy Lett.*, 2017, **2**, 2257.

[45] B. You, N. Jiang, M. Sheng, M. W. Bhushan and Y. Sun, *ACS Catal.*, 2016, **6**, 714.

[46] X. Xiao, C. T. He, S. Zhao, J. Li, W. Lin, Z. Yuan, Q. Zhang, S. Wang, L. Dai and D. Yu, *Energy Environ. Sci.,* 2017, **10**, 893.

[47] H. Liang, A. N. Gandi, C. Xia, M. N. Hedhili, D. H. Anjum, U. Schwingenschlögl and H. N. Alshareef, *ACS Energy Lett.*, 2017, **2**, 1035.

[48] X. Cui, P. Ren, D. Deng, J. Deng and X. Bao, *Energy Environ. Sci.*, 2016, **9**, 123.

[49] K. Fan, H. Chen, Y. Ji, H. Huang, P. M. Claesson, Q. Daniel, B. Philippe, H. Rensmo, F. Li, Y. Luo and L. Sun, *Nat. Commun.*, 2016, **7**, 11981.

[50] A. L. Strickler, M. Escudero-Escribano and T. F. Jaramillo, *Nano Lett.*, 2017, **17**, 6040.

[51] B. Zhang, X. Zheng, O. Voznyy, R. Comin, M. Bajdich, M. Garcia-Melchor, L. Han, J. Xu, M. Liu, L. Zheng, F. P. G. D. Arquer, C. T. Dinh, F. Fan, M. Yuan, E. Yassitepe, N. Chen, T. Regier, P. Liu. Y. Li, P. D. Luna, A. Janmohamed, H. L. Xin, H. Yang, A. Vojvodic and E. H. Sargent, *Science,* 2016, **352**, 333.

[52] X. Zheng, B. Zhang, P. D. Luna, Y. Liang, R. Comin, O. Voznyy, L. Han, F. P. Garcia de Arquer, M. Liu, C. T. Dinh, T. Regier, J. J. Dynes, S. He, H. L. Xin, H. Peng, D. Prendergast, X. Du and E. H. Sargent, *Nature Chem.,* 2018, **10**, 149.

[53] J. Li, Y. Wang, T. Zhou, H. Zhang, X. Sun, J. Tang, L. Zhang, A. M. Al-Enizi, Z. Yang and G. Zheng, *J. Am. Chem. Soc.*, 2015, **137**, 14305.

[54] L. Yu, H. Zhou, J. Sun, F. Qin, F. Yu, J. Bao, Y. Yu, S. Chen and Z. Ren, *Energy Environ. Sci*., 2017, **10**, 1820.

[55] X. Han, X. Wu, Y. Deng, J. Liu, J. Lu, C. Zhong and W. Hu, *Adv. Energy Mater*., 2018, 1800935.

[56] H. Liang, A. N. Gandi, D. H. Anjum, X. Wang, U. Schwingenschlögl and H. N. Alshareef, *Nano Lett.,* 2016, **16**, 7718.

[57] G. F. Chen, T. Y. Ma, Z. Q. Liu, N. Li, Y. Z. Su, K. Davey and S. Z. Qiao, *Adv. Funct. Mater*., 2016, **26**, 3314.

[58] E. Hu, Y. Feng, J. Nai, D. Zhao, Y. Hu and X. W. Lou, *Energy Environ. Sci.,* 2018, **11**, 872.

[59] N. Jiang, B. You, M. Sheng and Y. Sun, *Angew. Chem. Int. Ed*., 2015, **54**, 6251.

[60] J. Luo, J. H. Im, M. T. Mayer, M. Schreier, M. K. Nazeeruddin, N. G. Park, D. T. Tilley, H. J. Fan and M. Grätzel, *Science,* 2014, **345**, 1593.

[61] H. Wang, H. W. Lee, Y. Deng, Z. Lu, P. C. Hsu, Y. Liu, D. Lin and Y. Cui, *Nat. Commun*., 2015, **6**, 7261.

[62] K. Kobayashi and J. Yamauchi, *Phys. Rev. B,* 1995, **51**, 17085.

[63] C. Tsai, F. Abild-Pedersen and J. K. Norskov, *Nano Lett*., 2014, **14**, 1381.

[64] J. Kibsgaard, T. F. Jaramillo and F. Besenbacher, *Nat. Chem*., 2014, **6**, 248.
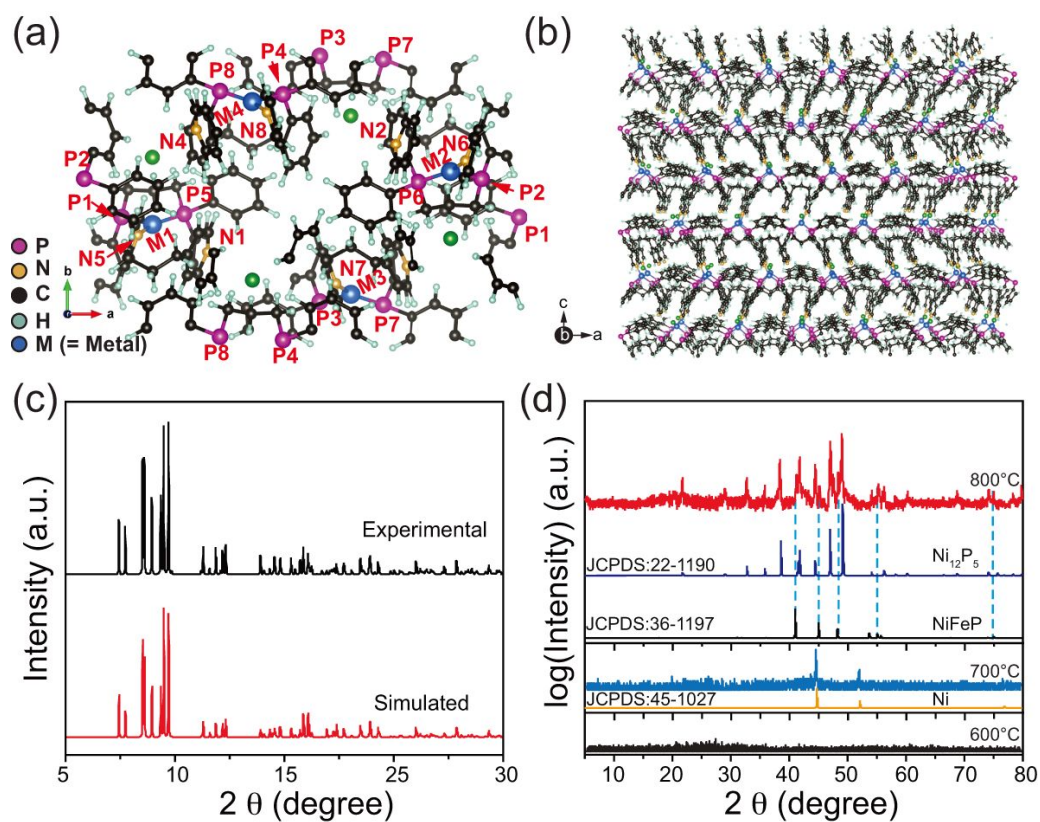
Fig. 1. (a) Unit-cell content of the crystal structure of the Ni/Fe-MOF with atoms labeled. Hydrogen and carbon atoms are not labeled for clarity. Green balls: open sites of TM bonded to C. (b) The crystal structure of Ni/Fe-MOF with 4 × 4 × 3 unit cells (b × c × a). (c) Experimental and simulated PXRD patterns of Ni/Fe-MOF. (d) XRD patterns of Ni/Fe-MOF samples pyrolyzed at 600, 700, and 800 °C, respectively. To better identify the various diffraction peaks, the XRD patterns are plotted in logarithmic scale. Reference diffraction patterns of standard Ni, $Ni_{12}P_5$, and NiFeP are also shown.
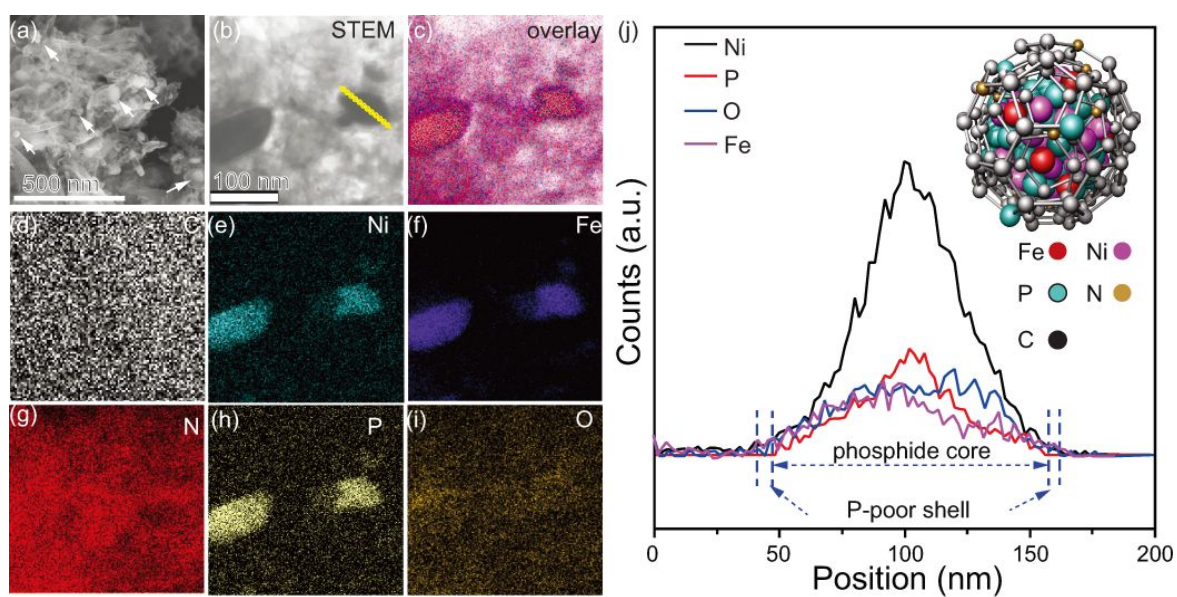
Fig. 2. Morphologies of the obtained NiP/NiFeP/C. (a) SEM image of NiP/NiFeP/C. (b) STEM image of NiP/NiFeP/C. (c) to (i) STEM-EDX elemental mapping of NiP/NiFeP/C. (j) STEM-EDX linear scanning of NiP/NiFeP/C. The scanning area is shown with the yellow lines in (b). The inserted image in (j) also shows the schematics of the composition of the NPs according to the STEM-EDX results.
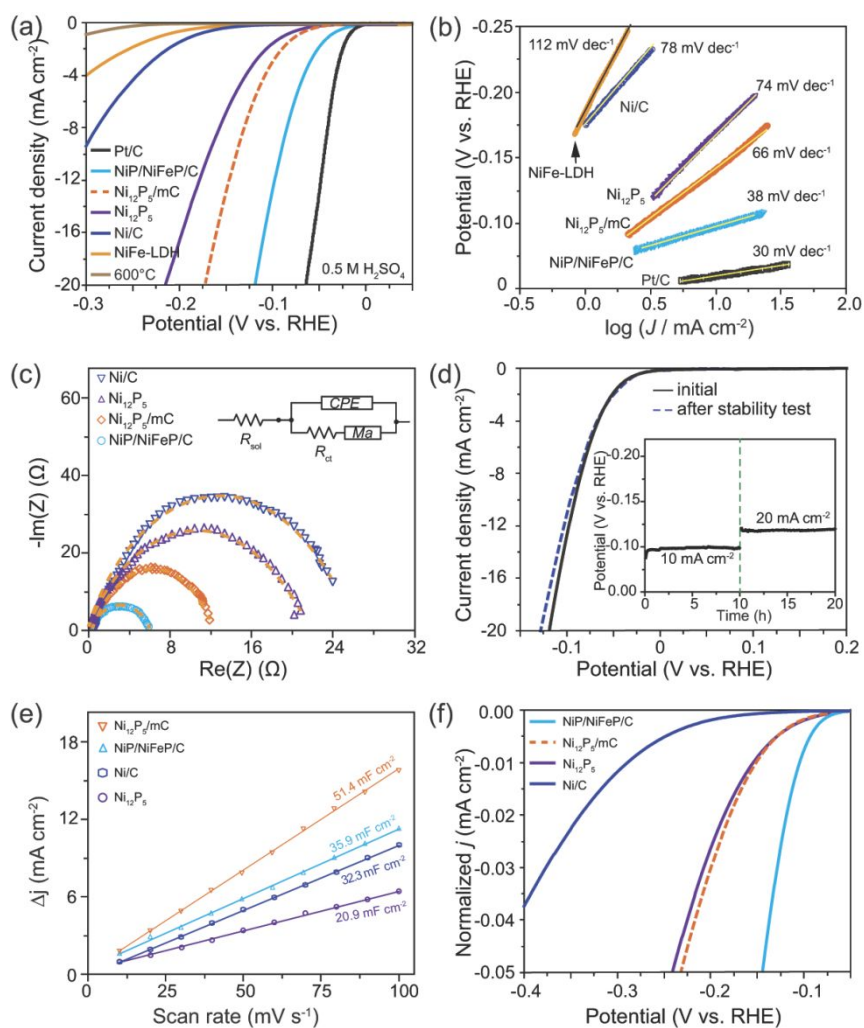
Fig. 3. (a) Polarization curves of NiP/NiFeP/C and the samples obtained by pyrolysis of Ni/Fe-MOF at 600 °C and 700 °C for HER in 0.5 M H_2SO_4. Pt/C, NiFe-LDH, NiP-mC, and NiP/C are also added for comparisons. (b) Corresponding Tafel plots of the samples shown in (a). (c) EIS curves of the NiP/NiFeP/C, NiP-mC, and NiP/C samples. Inserted circuit model: R_{sol}: resistance of solution, R_{ct}: charge transfer resistance, C_{dl}: double-layer capacitance. Dashed lines are the fitting curves according to the inserted circuit model. (d) Durability test for NiP/NiFeP/C sample. Inserted plot: polarization curves before and after galvanostatic tests at -10 mA cm^{-2} and -20 mA cm^{-2} for 20 h (insert plot). (e) The double-layer capacitance (C_{dl}) for NiP/NiFeP/C, NiP-mC, and NiP/C samples. (f) Polarization curves in (a) normalized by ECSA. ECSA was calculated according to A_{ECSA} = total specific capacitance/specific capacitance of per real surface area, while specific capacitance of per real surface area was estimated to be 40 µF cm^{-2} for most surfaces.[27]
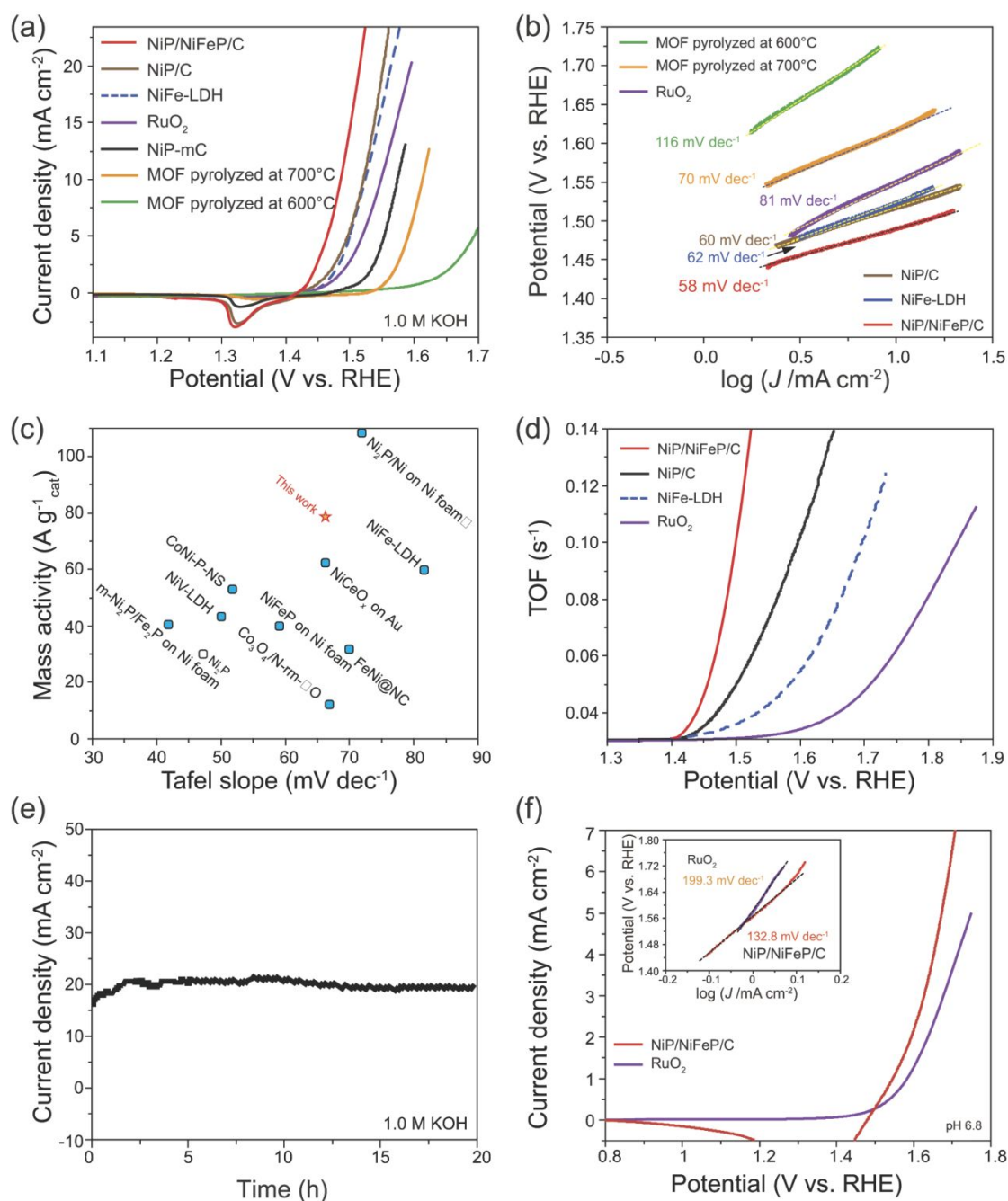
Fig. 4. Electrochemical characterizations of NiP/NiFeP/C and the samples obtained by pyrolysis of Ni/Fe-MOF at 600 °C and 700 °C for OER in 1.0 M KOH. RuO$_2$, NiFe-LDH, NiP-mC, and NiP/C are also added for comparisons. (a) Polarization curves. (b) Corresponding Tafel plots. (d) Comparison of the electrochemical activity (mass activity at 1.50 V (vs. RHE) and Tafel slopes) with the benchmark of reported phosphides and oxides, such as Ni$_2$P/Ni on Ni foam,[45] CoNi-P NSs,[46] NiFe-LDH,[6] NiCeO$_x$ on Au,[25] NiFeP on Ni foam,[47] FeNi@NC,[48] Co$_3$O$_4$/N-rm-GO,[11] Ni-V-LDH,[49] m-Ni$_2$P/Fe$_2$P on Ni foam,[44] and Ni$_2$P.[5] *: the mass loading was not provided, and the mass activity was estimated according to 2.0 mg cm^{-2}. (d) Calculated TOF plots for oxygen evolution. (e) Durability test for the NiP/NiFeP/C sample at 1.52 V (vs. RHE) for 20 h. (f) Polarization curves of NiP/NiFeP/C and RuO$_2$ in a phosphate buffer (pH 6.8) and their corresponding Tafel slopes (inserted plots).
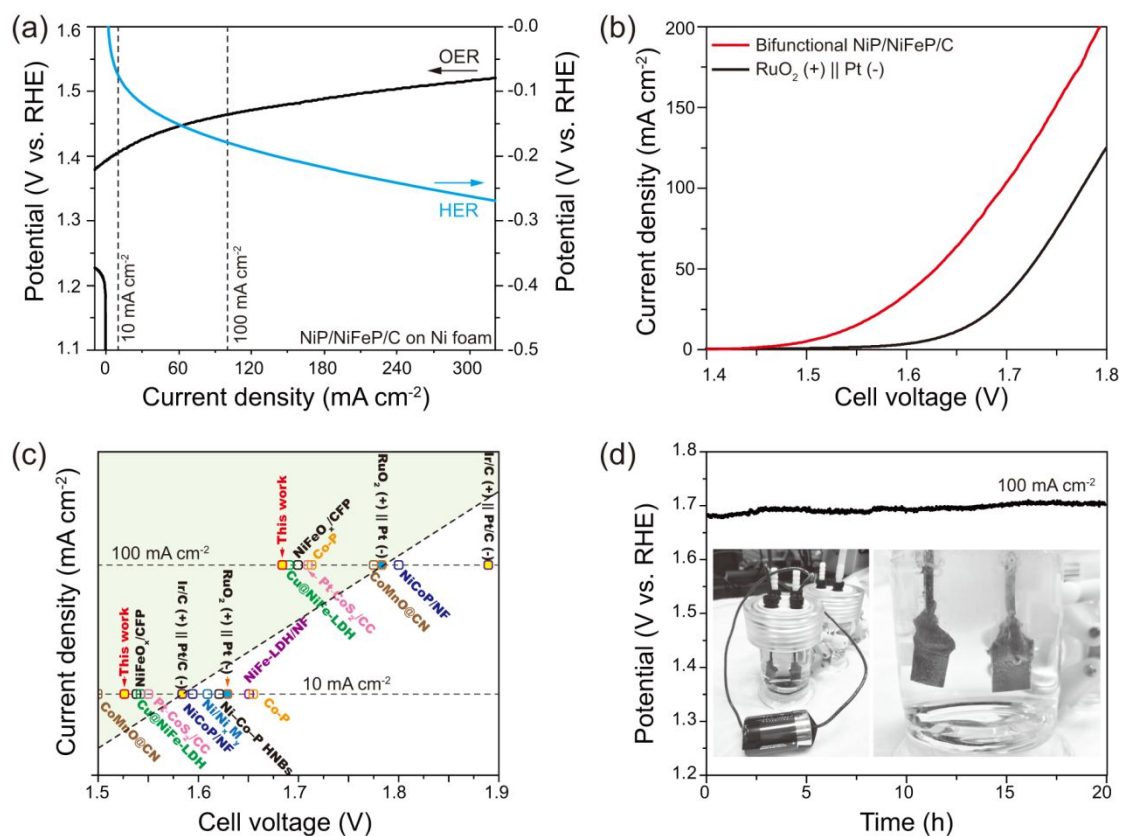
Fig. 5. Electrochemical characterizations of NiP/NiFeP/C-NiF for OER and HER as well as its overall water splitting performance as a bifunctional electrocatalyst in 1.0 M KOH. (a) Polarization curves for OER (black line) and HER (blue line). The absolute cathodic current densities of HER are used. (b) *J-V* curve of a two-electrode system composed of bifunctional NiP/NiFeP/C-NiF as the anode and the cathode (red line). A two-electrode water splitting system using noble metals (RuO_2 as the anode and Pt as the cathode) is also compared (black line). (c) Comparison of the electrochemical activities (cell voltage at 10 mA cm^{-2} and 100 mA cm^{-2}) with reported bifunctional electrocatalysts and noble metal pairs, such as CoMnO@CN,[53] Cu@NiFe-LDH,[54] Pt-CoS$_2$/CC,[55] NiCoP/NF,[56] Ni/Ni$_x$M$_y$,[57] Ni-Co-P HNBS,[58] Co-P,[59] NiFe-LDH/NF,[60] NiFeOx/CFP,[561] RuO$_2$(+)||Pt(-), and Ir/C(+)||Pt/C(-).[62] The dark area means that the activity is superior to that of the combinations of noble metal and its compounds. (d) Durability test of the overall water splitting system at 100 mA cm^{-2} for 20 h. Inserted photograph shows generation of H$_2$ and O$_2$ bubbles on the bifunctional NiP/NiFeP/C, powered by a 1.5 V D-type battery.